Eddy-Induced Diapycnal Fluxes and Their Role in the Maintenance of the Thermocline

TIMOUR RADKO AND JOHN MARSHALL

Department of Earth, Atmospheric, and Planetary Sciences, Massachusetts Institute of Technology, Cambridge, Massachusetts

(Manuscript received 6 August 2002, in final form 7 August 2003)

ABSTRACT

High-resolution numerical experiments are diagnosed to study the integral effects of geostrophic eddy fluxes on the large-scale ocean circulation. Three characteristic large-scale flows are considered: 1) an anticyclonic single gyre, 2) a double gyre, and 3) an unblocked zonal flow, a simple analog of the Antarctic Circumpolar Current. It is found that buoyancy and potential vorticity budgets in the presence of eddies are dominated by a balance between vertical advection into the control volume by Ekman pumping and eddy transfer across the density surfaces achieved by diapycnal eddy fluxes, with small-scale mixing making only a minor contribution. Possible oceanographic implications of the results are discussed.

1. Introduction

In this paper we discuss the role of time-dependent geostrophic eddy motions in the buoyancy and potential vorticity budgets diagnosed from numerical models of large-scale ocean flows. The ocean is full of energetic eddies that, as suggested by the numerical experiments herein, may be very effective in balancing global buoyancy and potential vorticity budgets. The possible role of eddies in this manner has been discussed in highly idealized laboratory and numerical studies by Marshall et al. (2002), Karsten et al. (2002), and Radko and Marshall (2003)—see also the discussion in Hughes (2002). Radko and Marshall (2003) considered an idealized abstraction of a subtrobical ocean gyre: the equilibration of a warm-pumped lens on a β plane. By construction, geostrophic eddies play a central role in the volume budget of the lens: warm fluid pumped down from the surface is fluxed away laterally by geostrophic eddies formed as a result of the baroclinic instability of a large-scale current in the region of western intensification.

Here we consider more complex and perhaps more realistic configurations in which the downward flux of buoyancy from the Ekman layer could either be balanced by eddies, explicit dissipation, or by advective fluxes. Three-dimensional eddy-resolving numerical experiments of ocean gyres are diagnosed to quantify the roles of eddy buoyancy, momentum, and potential vorticity transfer. While many previous eddy-resolving studies have focused on the properties of isopycnal eddy transfer and especially on the ability of eddies to mix potential vorticity (PV) or layer thickness (see, e.g., Drijfhout and Hazeleger 2001), in this paper we examine the role of eddies in balancing global buoyancy and potential vorticity budgets.

While eddies are often assumed to be largely adiabatic in the interior (e.g., Gent and McWilliams 1990), both theoretical reasoning and numerical simulation suggest that eddies have strong diabatic effects, particularly in near-surface frontal regions. Presence of the ocean surface tends to suppress the vertical component of the eddy fluxes $\overline{w'b'}$ (in standard notation) and thereby forces eddy fluxes to become nearly horizontal in regions where eddies ''feel'' the surface. As a result, eddy fluxes become directed across the isopycnals, resulting in significant diapycnal volume fluxes. We show here that these eddy-induced diapycnal fluxes may play a central role in balancing the downward Ekman flux of buoyancy and potential vorticity into the main thermocline.

Discussion in this paper is based on the diagnostics of idealized ocean models, which include a single gyre, a double gyre, and an unblocked zonal flow (in sections 2, 3, and 4, respectively). In each case we find that diapycnal eddy-induced fluxes play a dominant role in the buoyancy budget, with explicit diffusion making only a minor contribution. Likewise, we find that the *global* PV budget comprises, at leading order, a balance between downward potential vorticity flux due to Ekman pumping and lateral eddy transfer. Although the buoyancy and potential vorticity of a fluid particle can only be modified by small-scale dissipative processes, the dominance of the eddy transfer over explicit diffusion in the global time-mean budgets suggests that eddies facilitate irreversible transfer of properties in the cascade of vorticity and buoyancy to small scales.

Corresponding author address: Dr. Timour Radko, Dept. of Earth, Atmospheric, and Planetary Sciences, MIT, Bldg. 54-1517, 77 Massachusetts Avenue, Cambridge, MA 02139.
E-mail: timour@ocean.mit.edu

TABLE 1. Nondimensional parameters controlling dynamics of the time-mean flow in the numerical experiment. They are the Rossby number R_o, the aspect ratio of the domain R, Peclet numbers for the vertical (Pe_v) and horizontal (Pe_h) diffusion, Ekman numbers for the vertical (E_v) and horizontal (E_h) viscosity, and a measure of the β effect (β). Note that $U = \sqrt{(g'W_e)/f_0}$, and $H = [\sqrt{(f_0W_e)/g'}]L$.

$R_o = \frac{U}{f_oL}$	$R = \frac{L_y}{L}$	$\mathrm{Pe}_v = \frac{W_eH}{k_v}$	$\mathrm{Pe}_h = \frac{UL}{k_h}$	$E_v = \frac{\nu_v}{f_oH^2}$	$E_h = \frac{\nu_h}{f_oL^2}$	$\beta = \frac{\beta_{\mathrm{dim}}L}{f_o}$
0.9×10^{-3}	0.67	35	2×10^4	8×10^{-5}	2×10^{-6}	1.2

2. Preliminary calculations: Single-gyre experiment

The first type of flow studied is an idealized model of a subtropical gyre. Computations are made using the Massachusetts Institute of Technology general circulation model (MITgcm; Marshall et al. 1997a,b) in a rectangular box on whose walls normal flow is set to zero. A linear, one component (temperature) equation of state is used. Fluid is set in motion by applying a zonal wind stress that corresponds to the sinusoidal Ekman pumping velocity:

$$w_e = -W_e \sin(\pi y/L_y), \tag{1}$$

vanishing at the northern and southern boundaries of the basin. The initially unstratified fluid is also thermally forced by applying a uniform surface heat flux over a circular region in the western part of the basin; this results in a pattern of heat flux from the Ekman layer into the thermocline that is qualitatively similar to that observed in the North Atlantic subtropical gyre (e.g., Marshall et al. 1993, their Fig. 13).

The governing equations are nondimensionalized using the zonal extent of the basin (L), the value of the Coriolis parameter at the basin center (f_0), the (positive) maximum amplitude of the Ekman pumping (W_e), and the maximum value of buoyancy (g'). The corresponding scale of the horizontal velocity is $U = \sqrt{(g'W_e)/f_0}$, and $H = [\sqrt{(f_0W_e)/g'}]L$ is the vertical scale. The structure of the resulting nondimensional equations indicates that the dynamics of the time-mean flow is governed by the set of nondimensional parameters listed, using conventional notation, in Table 1. The values of the key parameters used in the single-gyre experiment in Table 1 are close to those employed in Radko and Marshall (2003) and in Marshall et al. (2002). These numbers describe a relatively small basin ($L \approx 35R_d$), and other control parameters are correspondingly rescaled relative to typical oceanic values.

For the dimensional oceanic scales of $f_0 \sim 10^{-4}\ \mathrm{s}^{-1}$, $L \sim 2 \times 10^6$ m, $W_e \sim 50$ m yr^{-1}, and $g' \sim 10^{-2}$ m s^{-2}, the employed uniform vertical diffusivity is equivalent to $k_v = W_eH/\mathrm{Pe}_v \sim 10^{-5}\ \mathrm{m}^2\ \mathrm{s}^{-1}$, which is consistent with the values suggested by microstructure and tracer release measurements in the main thermocline (e.g., Ledwell et al. 1993). The chosen depth of the basin exceeds the (anticipated) thermocline depth by a factor of 5, so as to roughly approximate the situation in oceanic gyres. Flow is discretized on a uniform mesh with $150 \times 100 \times 40$ elements, and the Ekman layer is resolved by three grid points. A no-stress condition is employed at the lateral boundaries, and a no-slip condition is used at the bottom. Since the baroclinic radius of deformation (R_d) in the resulting solutions is much smaller than the scale of the flow ($L = 1.5L_y \sim 35R_d$), the mean flow is baroclinically unstable. At the same time, R_d is reasonably well resolved by our numerical grid, which makes it possible to adequately represent baroclinic instability and the resulting geostrophic eddy field.

The model was initialized from rest with water of uniform temperature. After a few rotation periods a mechanically driven barotropic circulation was established. However, the time scale associated with the setup and equilibration of the baroclinic flow is much larger [$\sim 10^4/(2\pi)$ rotation periods]. Figure 1a shows a typical instantaneous temperature field for a fully developed quasi-equilibrated eddying gyre. Baroclinic instability manifests itself in the continuous formation of irregular eddies that carry warm fluid laterally across the sloping isopycnals. A quasi-steady state is achieved when the rate of the diapycnal buoyancy transport by eddies becomes equal to the buoyancy flux at the surface, as discussed for the case of the warm-pumped lens on the β plane in Radko and Marshall (2003). It should be noted that because of the absence of a balancing heat sink in this single-gyre circulation, we can only reach a quasi-steady equilibrium. However, this undesirable feature has no significant dynamical consequences in our model since the overall temperature increase over the duration of the experiment is much less than its spatial variation.

The time-mean temperature field in Fig. 1b is markedly different from the irregular and disorganized instantaneous picture in Fig. 1a; the circulation pattern in Fig. 1b consists of a Sverdrup-type interior flow bounded on the west by a narrow intensification region. The vertical cross section in Fig. 1c reveals the nature of the dynamical questions raised in the introduction. Ekman pumping drives buoyant (large b), stratified (high PV) fluid down into the main thermocline. The existence of a steady state demands that, for *each* time-mean isotherm, the influx of PV and buoyancy from the Ekman layer is balanced by the cross-layer fluxes. Our goal is to identify the origin of these diapycnal fluxes and quantify their role in balancing the buoyancy and PV budgets.

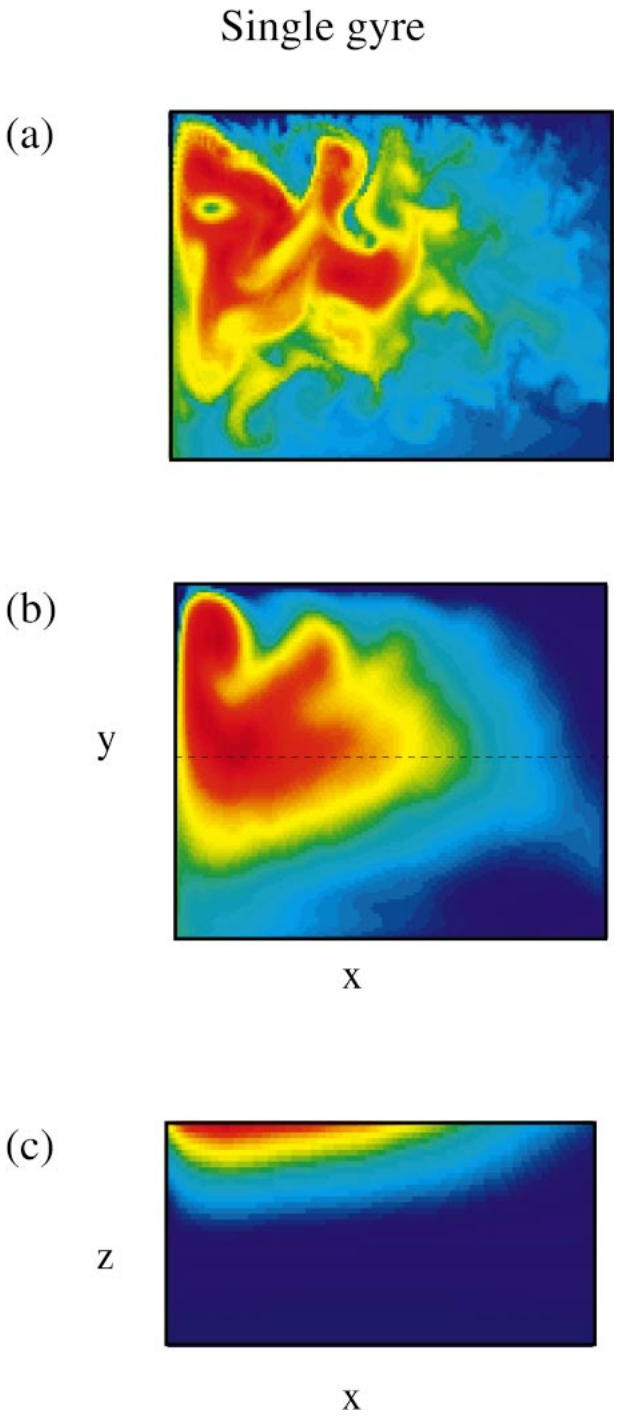

FIG. 1. Horizontal (a) instantaneous and (b) time-mean cross sections of the temperature field immediately below the Ekman layer. (c) Vertical section of the time-mean flow at middomain, along the dashed line in (b).

a. Time-mean equations

In order to analyze the balances that occur in the statistically steady numerical solutions considered herein, the governing equations are written for time-mean quantities thus:

$$u\frac{\partial u}{\partial x} + v\frac{\partial u}{\partial y} + w\frac{\partial u}{\partial z} - fv = -\frac{\partial p}{\partial x} + M_u + F_u,$$

$$u\frac{\partial v}{\partial x} + v\frac{\partial v}{\partial y} + w\frac{\partial v}{\partial z} + fu = -\frac{\partial p}{\partial y} + M_v + F_v,$$

$$b = \frac{\partial p}{\partial z},$$

$$\frac{\partial u}{\partial x} + \frac{\partial v}{\partial y} + \frac{\partial w}{\partial z} = 0, \quad \text{and}$$

$$u\frac{\partial}{\partial x}b + v\frac{\partial}{\partial y}b + w\frac{\partial}{\partial z}b = D + B, \tag{2}$$

where (u, v, w, b, p) are, respectively, the time-mean velocity components, buoyancy, and pressure. Small-scale mixing processes in the ocean are represented by B, which includes the explicit [parameterized as $k_v(\partial^2 b/\partial z^2)$] and implicit numerical vertical diffusion. Momentum transfer by unresolved scales (represented by numerical viscosity) is given by $\mathbf{F}$, which, we assume and subsequently verify, is negligible outside of top and bottom Ekman layers and lateral viscous sublayers near the basin boundaries. Reynolds stress terms are given by (M_u, M_v), and D is the buoyancy eddy-transfer term, given by

$$M_u = -\left(\frac{\partial\overline{u'^2}}{\partial x} + \frac{\partial\overline{u'v'}}{\partial y} + \frac{\partial\overline{u'w'}}{\partial z}\right),$$

$$M_v = -\left(\frac{\partial\overline{v'u'}}{\partial x} + \frac{\partial\overline{v'^2}}{\partial y} + \frac{\partial\overline{v'w'}}{\partial z}\right), \quad \text{and}$$

$$D = -\left[\frac{\partial}{\partial x}(\overline{u'b'}) + \frac{\partial}{\partial y}(\overline{v'b'}) + \frac{\partial}{\partial z}(\overline{w'b'})\right]. \tag{3}$$

The overbars denote a time average at a fixed point in space, and primes pertain to the eddy fields.

b. Buoyancy

The discussion of the buoyancy dynamics is phrased in terms of the cross-isopycnal volume flux $w^* = (D + B)/b_z$; this measure of the strength of the diapycnal transfer was employed in Radko and Marshall (2003) and is discussed in the appendix [see (A3)]. The first question to be addressed is whether w^* in our calculations is dominated by eddies or by numerical diffusion, explicit or implicit.[1] Consider a control volume (V_T) bounded by the base of the Ekman layer on top and by one of the time-mean isotherms (T_s) from below. The rate of pumping of the incompressible fluid into this

[1] The total diapycnal volume flux w^* should not be confused with the vertical eddy velocity of residual mean theory—a very different quantity, which is also often denoted by the same symbol.

control volume from the Ekman layer is equal, in a steady state, to the total volume flux across its lower surface:

$$\iint w_e \, dx \, dy = \iint w^* \, dx \, dy,$$

where w^* is evaluated on the isotherm (by linearly interpolating the variables), and the integration is carried over the surface bounded by the outcrop of this isotherm.

The contribution to w^* due to eddies is given by

$$w^*_{\text{eddies}} = D\left(\frac{\partial b}{\partial z}\right)^{-1}.$$

Thus, a meaningful measure of the relative importance of eddies is given by the parameter

$$\alpha = \frac{\iint w^*_{\text{eddies}} \, dx \, dy}{\iint w^*_{\text{total}} \, dx \, dy} = \frac{\iint D b_z^{-1} \, dx \, dy}{\iint w_e \, dx \, dy}. \quad (4)$$

To be specific, we now return to the mean flow in Figs. 1b,c and consider the isotherm whose temperature is $T_s = 0.5(T_{\max} + T_{\min})$; $T_{\max}$ and $T_{\min}$ are, respectively, the maximum and minimum temperature at the base of the Ekman layer. When the expression in (4) is diagnosed from the direct numerical simulations, we find that

$$\alpha_{1/2} = 0.85.$$

Thus, the explicit diffusivity, representing small-scale processes in the model, accounts for only a fraction of the cross-isopycnal buoyancy flux for the median isotherm T_s; values of α are even higher for the more shallow isotherms. This is a key result of our study. Diagnostics based on this integral measure (α) will be used to quantify the role of eddies in each of our model configurations (sections 3 and 4). It is shown in the appendix that $\alpha \to 1$ can only be realized if the eddies have a diapycnal component, that is, if $\overline{\mathbf{v}'b'} \cdot \nabla b \neq 0$.

The above diagnostics revealed the significance of eddy transfer in balancing the buoyancy and volume budgets. We now wish to determine whether the same holds for the balances involving potential vorticity, which is directly connected to the circulation dynamics (e.g., Rhines 1993).

c. Potential vorticity

To quantify the integral contribution of eddies in balancing the vorticity continuously imparted by winds, we use the integral form of the large-scale potential vorticity equation derived in the appendix [(A13)]:

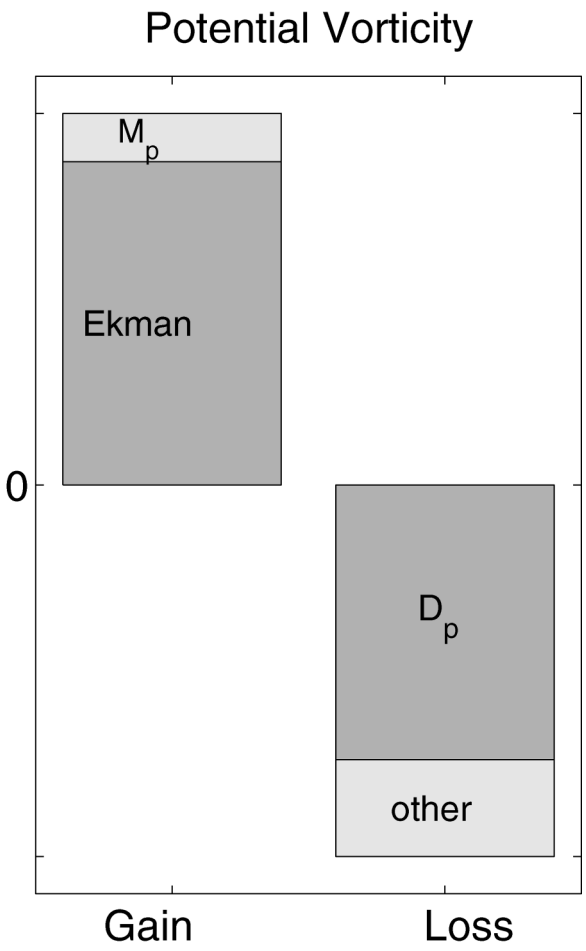

FIG. 2. Histograms of the potential vorticity budget. The downward PV flux from the Ekman layer is approximately balanced by the eddy buoyancy transfer (D term).

$$\iint Q w_e \, dx \, dy = \iiint M_p \, dV + \iiint D_p \, dV + \text{other terms}, \quad (5)$$

where $Q = (f\mathbf{k} + \nabla \times \mathbf{v}) \cdot \nabla b$ is the large-scale potential vorticity, and $M_p = (\nabla \times M) \cdot \nabla b$ and $D_p = (\nabla \times \mathbf{v} + f\mathbf{k}) \cdot \nabla D$ represent the components of the advective variation in the potential vorticity from the eddy momentum and buoyancy transfer, respectively.

The rectangular control volume (Fig. A1) for which we apply (5) is slightly ($\delta = L/50$) separated from the boundaries of the basin to exclude the thin sublayers that are controlled by explicit diffusivity and viscosity. The ''other terms'' thus include diffusive and viscous effects in the interior and lateral fluxes into sublayers near the vertical boundaries. The balance of the various terms in (5) is shown in a histogram in Fig. 2. We see that the surface forcing is essentially balanced by the eddy buoyancy transfer term (D_p). Note that the other terms account for just a fraction of the total PV budget.

The momentum transfer (M_p) is also rather weak and, furthermore, acts to increase the PV. Since the control volume (see Fig. A1) is large enough to include all the major features of the circulation, the PV budget in Fig. 2 can be used, we argue, as an objective integral measure of the significance of diabatic factors affecting the dynamics of the flow in the gyre interior.

Inspection of the spatial (x, y) distribution (not shown) of the vertically integrated M_p and D_p terms in (5) indicates that the momentum and buoyancy transfer effects are mostly limited to the northwest corner of the basin. This feature is consistent with oceanic observations that show enhanced eddy activity in the vicinity of the strong western boundary currents. The localized nature of eddy effects justifies use of ideal thermocline models as a zero-order description of the ocean interior in the presence of eddies.

Calculations discussed in this section demonstrated that eddy transfer of buoyancy plays a consistently dominant role in several important balances involving the potential vorticity and buoyancy dynamics of the single-gyre circulation. We now turn to a more complicated and, perhaps, more realistic system consisting of two symmetric gyres. In addition to the eddy effects represented in the single-gyre model, the dynamical balances of the double-gyre system can also be affected by the advective intergyre flows (e.g., Chen and Dewar 1993).

3. Double-gyre experiment

We now consider a double-gyre system forced by a zonal wind stress [$\tau = -W_e f \cos(2\pi y/L_y) L_y/(2\pi)$], which corresponds to the antisymmetric Ekman velocity,

$$w_e = -W_e \sin(2\pi y/L_y),$$

negative over the southern half of the rectangular basin ($0 < y < L_y/2$) and positive over the northern half ($L_y/2 < y < L_y$).[2] The fluid is also thermally forced by slowly, on a time scale of $10^4 f^{-1}$, relaxing the surface temperature in the subtropical (subpolar) gyre to the uniform temperature T_S (T_N) except for a thin ($L_y/20$) intergyre region where relaxation is not applied. The chosen difference in the target temperatures $\Delta T = T_S - T_N = 10°C$ is such that the first baroclinic radius of deformation in the resulting flow is considerably less than the basin scale but resolved in the numerical solutions, thus permitting capture of baroclinic instability and ensuing eddy transfer.

The fluid was spun up from a state of rest and uniform temperature (T_N). The general features of the flow evolution are similar to those observed in the single-gyre experiment (section 2). First the barotropic circulation is set up by the wind, followed by creation of a buoyant pool in the southern half of the basin by thermal forcing. The thermal front at the intersection of the gyres soon becomes baroclinically unstable, generating irregular eddies as shown in the horizontal temperature cross section in Fig. 3a. Since there is no net input of vorticity and heat into the basin, the flow eventually reaches a true statistical equilibrium: the corresponding time-mean temperature field is plotted in Fig. 3b. One of the striking features of the solution in Fig. 3b is a very sharp and well-defined thermal front, which separates

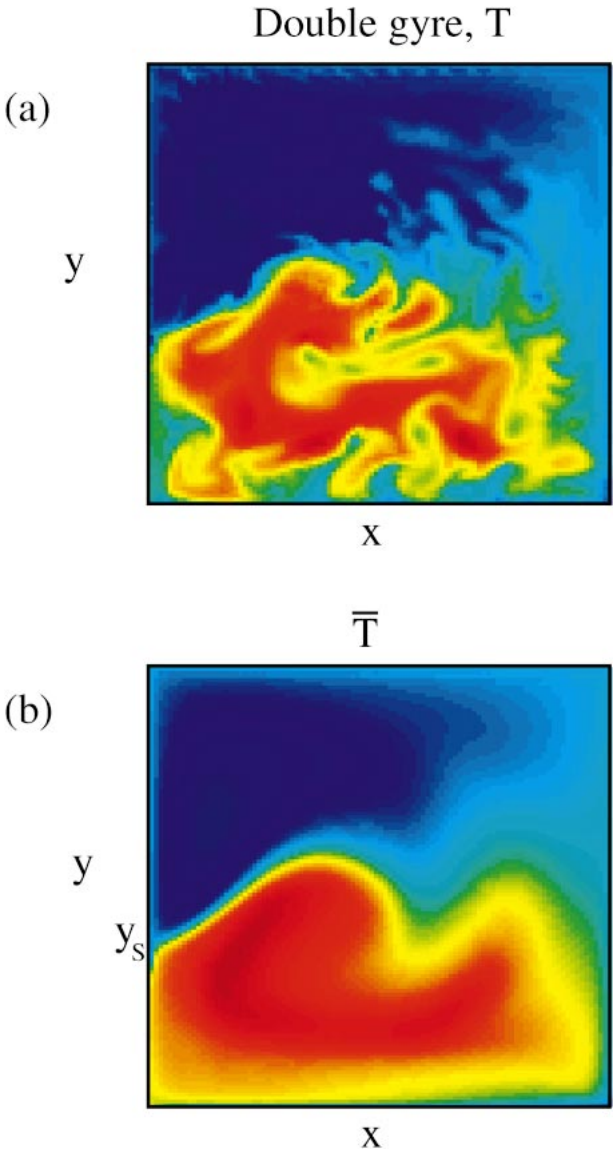

FIG. 3. Horizontal cross section of the temperature at the base of the Ekman layer in the double-gyre numerical experiment: (a) typical instantaneous picture and (b) time-mean temperature.

[2] This experiment can be regarded as an extension of the barotropic double-gyre model studied by Marshall (1984) to a mechanically and thermally forced system. Marshall's barotropic calculation demonstrated that the eddies can establish an equilibrium state simply by fluxing vorticity between gyres in an amount equal to that put in by wind.

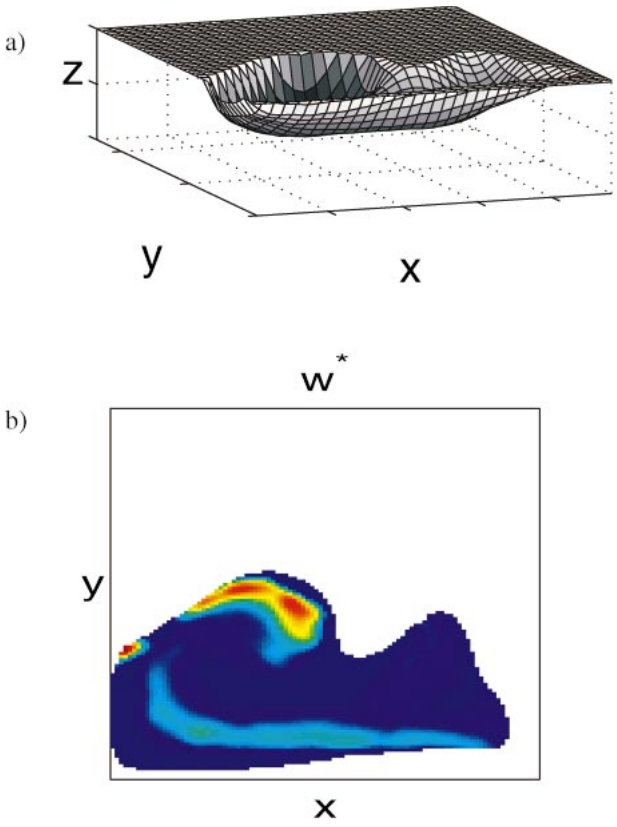

FIG. 4. (a) Spatial structure of the time-mean isotherm $T_s = 0.5(T_{max} + T_{min})$. (b) Distribution of the cross-isopycnal eddy transfer (w^*) for the isotherm shown in (a). Red color corresponds to the high values of w^*, whereas the areas with low buoyancy transfer are shown in blue.

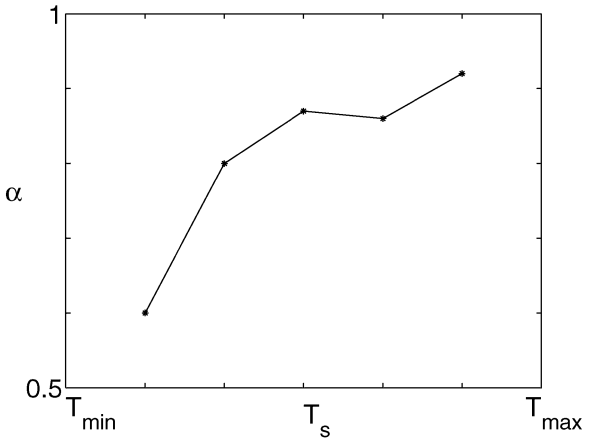

FIG. 5. The eddy-induced cross-isopycnal volume flux is normalized by the total flux [see (4)] and plotted as a function of the temperature T_s. The diapycnal volume flux is dominated by the contribution from eddies for most of isopycnal surfaces T_s in the interval $T_{min} < T_s < T_{max}$.

from the western boundary at the point $y = y_s$ somewhat to the south of the zero Ekman pumping line. Such behavior may be associated with the Parsons (1969) effect, which attributes Gulf Stream separation to a balance between Ekman and geostrophic meridional volume transports.

a. Buoyancy budget

To assess the role of eddies in maintenance of the subtropical thermocline, we computed, as in section 2, the partitioning of the diapycnal fluxes between eddy driven and diffusive processes for the median isotherm $T_s = 0.5(T_{max} + T_{min})$ shown in Fig. 4a. As before, T_{min} (T_{max}) is the minimum (maximum) temperature at the base of the Ekman layer, and w^*_{total} was obtained by integrating the Ekman flux over the surface area bounded by the outcrop (see Fig. 4). We find a flux ratio of

$$\alpha_{1/2} = \frac{w^*_{eddies}}{w^*_{total}} = 0.87,$$

which reveals the central role of eddies in establishing an equilibrium and maintenance of the model thermocline. Maps of w^*_{eddies} on the isopycnals (e.g., Fig. 4b) reveal the localized nature of eddy transport that is greatly enhanced in the vicinity of the swift and energetic time-mean current separating subpolar and subtropical gyres. The normalized cross-isopycnal eddy flux α has also been computed for other isopycnal surfaces; for those that intersect the lateral boundaries, it becomes necessary to include the advective fluxes from the thin lateral sublayers. Figure 5 plots α as a function of T_s and clearly indicates that the primary balance is between Ekman pumping of warm water into the subtropical thermocline and eddy-induced diapycnal flux across isopycnals, with vertical diffusion playing a significantly lesser role for all mean density surfaces.

The results in Fig. 5 should be contrasted with more conventional measures of eddy transfer. For example, the basin-averaged meridional eddy heat flux $\langle \overline{v'T'} \rangle$ accounts for only 25% of the total meridional heat flux $\langle vT + \overline{v'T'} \rangle$ in the experiment in Figs. 3 and 4. Such a moderate role of eddies in the direct meridional heat transport is consistent with the results of other eddy-resolving numerical simulations focused on the partitioning of the meridional fluxes in the Atlantic and Pacific basins, summarized in a review article by Bryan (1996). Our results, however, emphasize a different aspect of eddy transfer. We suggest that a fundamental role of eddies, and an important large-scale consequence, is related to their ability to induce *diapycnal* fluxes, essential to the maintenance of the thermocline.

b. Potential vorticity budget

Consider the PV budget of the subtropical gyre in the double-gyre model. We employ a rectangular control volume $V = (x_1, x_2) \times (y_1, y_2) \times (z_1, z_2)$, which is slightly separated from the rigid boundaries to avoid consideration of the thin sublayers governed by explicit

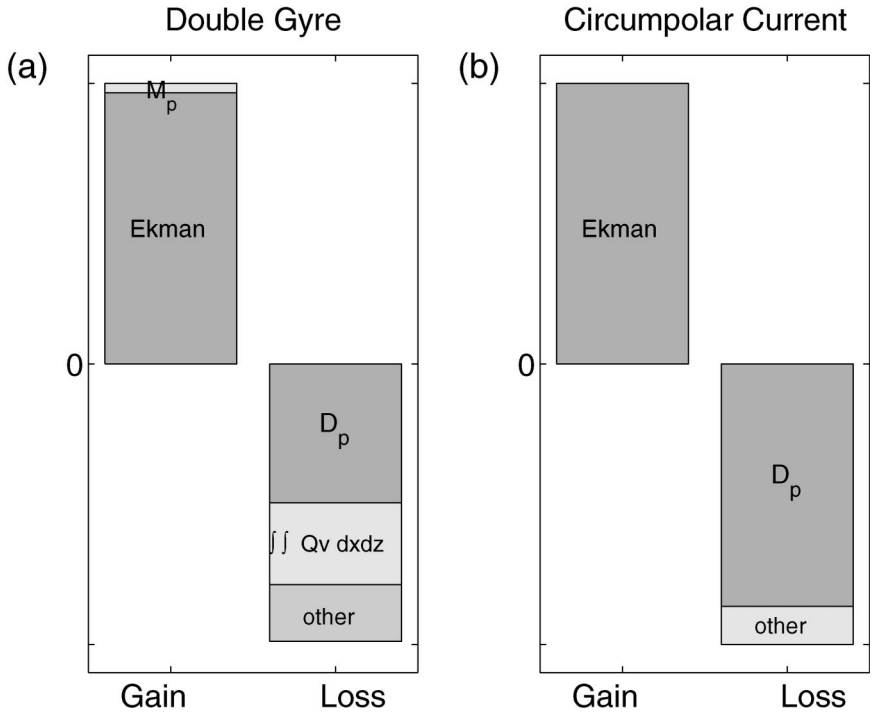

FIG. 6. Partitioning of the PV sources and sinks for the vorticity budget in the (a) double-gyre and (b) circumpolar current experiments.

dissipation. The northern boundary is placed at the separation point of the boundary current in Fig. 3b: $y_2 = y_s$. Thus, in addition to eddy transfer, the integral potential vorticity budget [(A13)] is now affected by mean advection of the PV through the northern boundary of the control volume, given by $\iint Qv\, dx\, dz$.

Components of the PV budget have been diagnosed from the direct numerical simulation and plotted in Fig. 6a. These integral characteristics indicate that, although there is significant advection of potential vorticity out of the control volume V by the mean field, the eddy-induced transfer (D_p term) makes a more significant contribution. Comparison of the momentum and buoyancy eddy transfer terms in Fig. 6a shows that the dynamical influence of the former process is almost negligible (as in the single-gyre model).

Potential vorticity diagnostics have also been applied to a different control volume V_T, defined as a water mass below the Ekman layer whose temperature exceeds the average $T_2 = 0.5(T_{\max} + T_{\min})$—this is the isopycnal shown in Fig. 4a. The result for this control volume,

$$\frac{\iiint M_p\, dV}{\iiint D_p\, dV} = -0.044, \tag{6}$$

shows that the buoyancy transfer mechanism is the most efficient in modifying the large-scale potential vorticity. The spatial (x, y) distribution of the vertically integrated PV sources and sinks $\int M_p\, dz$ and $\int D_p\, dz$ is shown in Fig. 7. It is interesting to note that, although the average value of the Reynolds stress term (M_p) in the thermocline is much less than the corresponding buoyancy transfer term (D_p), as (6) indicates, the maximum amplitudes of $\int M_p\, dz$ and $\int D_p\, dz$ are comparable (these are plotted in Fig. 7 using the same contour interval). Thus, *locally*, the Reynolds stress terms may have important dynamical consequences.

An important question arises at this point as to why the momentum transport plays only a secondary role in the PV balance. This can be rationalized by a simple order-of-magnitude estimate of D_p and M_p terms, which yields, assuming the geostrophic scaling,

$$M_p \sim \frac{M}{L}\frac{b}{H} \sim \frac{U'^2}{L_{\text{local}}}\frac{fU_{\text{local}}}{H^2},$$

$$D_P \sim f\frac{D}{H} \sim \frac{U'b'}{L_{\text{local}}}\frac{f}{H} \sim \frac{U'^2 f^2}{H^2}, \quad \text{and}$$

$$\frac{M_p}{D_p} \sim \frac{U_{\text{local}}}{fL_{\text{local}}} = R_{\text{olocal}}, \tag{7}$$

where U_{local}, L_{local}, and R_{olocal} are the local scales for the time-mean velocity, spatial scales, and Rossby number. This scaling argument is certainly relevant for single- and double-gyre models, as well as for the following zonal jet experiment. Because the ratio of the two effects

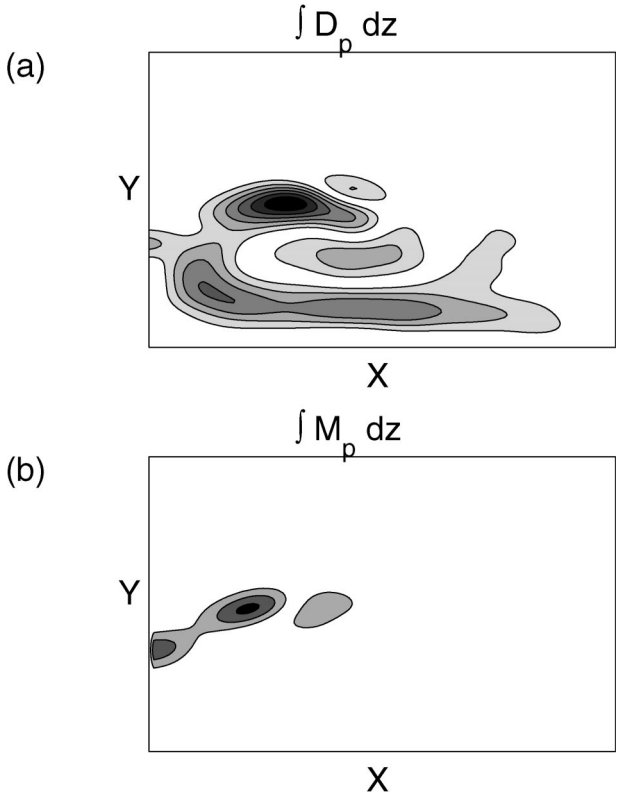

FIG. 7. Spatial distribution of the vertically integrated sources and sinks of the potential vorticity: (a) component related to the eddy buoyancy transfer and (b) component due to the Reynolds stresses. Regions with high absolute values are indicated by dark shading.

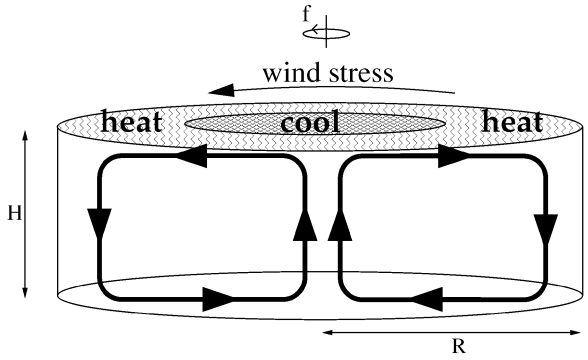

FIG. 8. Schematic diagram of the ACC experiment (from Karsten et al. 2002). The net surface heating, integrated over the domain, vanishes.

is proportional to the local Rossby number (not to be confused with its nominal value in Table 1), in the integral PV budgets the relevant Rossby number should be based on the scales in the western intensification zone since that is the location of the most intense eddy shedding. Although the Rossby number in the western intensification zone is nonnegligible, its numerical value is still significantly less than unity ($\sim$0.1), which explains the observed balance in Figs. 2 and 6a.

4. Circumpolar current experiments

The final example considered is a model of the Antarctic Circumpolar Current (ACC). The absence of zonal land barriers results in the distinct dynamical features that have no direct counterpart in gyre circulation, and the reader is referred to a review by Rintoul et al. (2001) for a comprehensive discussion of the ACC dynamics. In this section we revisit a highly idealized model of the Antarctic Circumpolar Current studied by Karsten et al. (2002). The setup used is shown in the schematic diagram Fig. 8. A cylinder of fluid is forced at the surface by an azimuthal wind stress and heated/cooled from above. One of the significant limitations of this model is related to the use of the f-plane approximation—latitudinal variation of the Coriolis parameter is ignored at this level of analysis. The buoyancy forcing (see Fig. 8) corresponds to heating in the annulus region $\frac{1}{2}R < r < R$ and cooling in the central part ($0 < r < \frac{1}{2}R$) such that no net buoyancy is added to the fluid. The experiment was spun up from rest beginning with water of uniform temperature. The reader is referred to Karsten et al. (2002) for details of the experimental setup. The numerical data in Karsten et al. (2002) are now used to examine the mechanism of the interaction between the eddies and the mean field and the location of the significant eddy induced effects, as inferred from sources and sinks of the large-scale PV.

The mean flow in the exterior region ($\frac{1}{2}R < r < R$), where the water is heated and pumped down, is markedly different from that in the central area where water is cooled (see Fig. 6 in Karsten et al. 2002). Stratification (and hence PV) is much higher below the heating zone, implying a finite net flux of mean-field PV from the Ekman layer into the interior. Thus, in a steady state, there must be a balancing sink of PV outside of the Ekman layer. In order to understand what causes such an internal loss of PV we apply the integral form of the PV equation [(A11)] to the control volume outside of the top and bottom Ekman layers.

Diagnostics of Karsten's numerical simulations lead to the integral PV budget in Fig. 6b. Again, the dominant balance is between the PV flux at the base of the Ekman layer and the eddy transfer in the interior. The Reynolds stress term M_p is not shown in Fig. 6b since it turned out to be two orders of magnitude less than the D term. Such a minor role of the Reynolds stress in ACC dynamics can be rationalized from the estimate in (7). Unlike the gyre problems, which are characterized by the presence of intense inertial western boundary currents with significant [$O(0.1)$] Rossby number, the ACC flow is much more homogeneous, and the Rossby number is uniformly low ($R_{\text{olocal}} \lesssim 10^{-3}$). As a result, as follows from (7), the momentum transfer is far less significant in the ACC model than it is for the gyres.

The spatial distribution of the internal sinks of PV is shown in Fig. 9. In this figure we took advantage of the

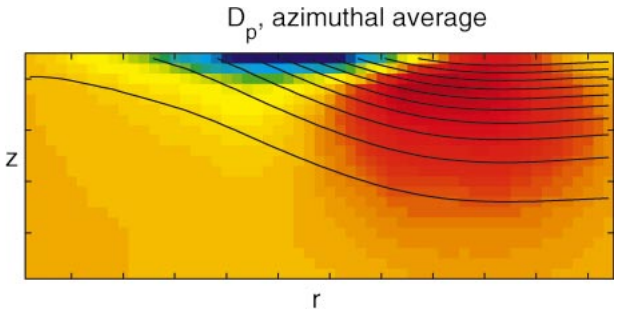

FIG. 9. Spatial distribution of the internal PV sinks due to eddy buoyancy transfer. Azimuthal average of the D term is plotted as a function of r and z (red corresponds to large negative D_p). Solid lines represent the time-mean isotherms.

radial symmetry in our problem and plotted the azimuthally averaged D_p term as a function of (r, z). This diagnostic indicates that most of the eddy-mean field interaction, as expressed in terms of PV dynamics, occurs in a narrow annular region below the Ekman layer in the external ($\frac{1}{2}R < r < R$) part of the basin. That is, the region where large convergence of the advective downward fluxes of PV has to be balanced by eddy-induced circulation, which tends to mix the high PV fluid in the equatorward (large r) part of the basin with the cold, low-PV fluid in the polar (small r) regions.

5. Conclusions and discussion

In this paper we have examined the role of eddies in the buoyancy and potential vorticity budgets of eddying large-scale flows. Three different oceanic scenarios have been considered that include single- and double-gyre β-plane flows and a circumpolar f-plane current. In each case we diagnosed eddy-resolving numerical simulations and determined the key processes affecting the mean buoyancy and potential vorticity budgets. Although the specific balances that quantify the evolution of the mean buoyancy and PV budgets differ from case to case, as summarized in Table 2, some features appear to be robust and are not model dependent. In particular, in all cases the downward flux of buoyancy and PV from the Ekman layer into the main thermocline is largely balanced by eddy buoyancy transfer (second and fourth columns in Table 2).

The dominance of eddy transfer in the integral buoyancy and PV budgets (Table 2) can be attributed to the diabatic component of eddy transfer (see the appendix for further discussion). While eddies may be largely adiabatic in the interior, proximity of the surface tends to suppress the vertical component of motion, forcing the eddies to transfer buoyancy across isopycnals in the upper ocean. This localized diabatic effect results in diapycnal volume fluxes (w^*), which are sufficient to balance the Ekman pumping into the main thermocline. This is in contrast to the study of, for example, McWilliams et al. (1996) who parameterized eddies with an adiabatic scheme and found that the input of buoyancy was mostly balanced by an interior diffusive flux. Instead, the resolved eddies in our experiments are essential in warm water budgets, dominating the parameterized microstructure contributions.

TABLE 2. Summary of the diagnostics for the three oceanic scenarios considered. Vorticity balances in the second and third column pertain to the control volume outside of the top and bottom Ekman layers, whereas the buoyancy parameter α (last column) corresponds to the fluxes across the isotherm with $T_s = 0.5(T_{max} + T_{min})$.

	$\dfrac{\iiint D_p\, dV}{\iint Qw_{Ek}\, dx\, dy}$	$\dfrac{\iiint M_p\, dV}{\iiint D_p\, dV}$	$\alpha = \dfrac{w^*_{eddies}}{w^*_{total}}$
Single gyre	0.85	0.176	0.85
Double gyre	0.5	0.064	0.87
ACC	0.87	0.018	0.98

In summary, based on our analysis of eddy-resolving idealized models, we find that

1) the direct effect of small-scale diffusion on the time-mean fields is much less than that of eddy transfer, at least in the *global* buoyancy and PV budgets for the upper layers;
2) the dynamically significant eddy fluxes are localized to frontal regions, the western intensification zones of oceanic gyres and circumpolar jets; and
3) the integral contribution of eddies to the large-scale PV budget is associated with the eddy buoyancy transfer (w^* effect), rather than Reynolds stress.

Acknowledgments. We thank the Physical Oceanography Division of the National Science Foundation, whose support made this study possible.

APPENDIX

Diagnostic Framework

a. Buoyancy transfer

Consider the buoyancy equation [(2)]. Both eddies [D term in (2)] and small-scale mixing [B term in (2)] result in a flow across the time-mean buoyancy surfaces, which we denoted below by w^*. In a statistically steady state w^* can be conveniently expressed in terms of D and B by rewriting the equations of motion using buoyancy (rather than z) as a vertical coordinate:

$$w^* = w(x, y, b) - \frac{D}{Dt}z(b)$$

$$= w - \left[u\frac{\partial}{\partial x}z(b) + v\frac{\partial}{\partial y}z(b)\right]. \qquad \text{(A1)}$$

Equation (A1) is further simplified using the expression for the isopycnal slope in z coordinates:

$$\frac{\partial}{\partial x}z(b) = -\frac{b_x}{b_z} \quad \text{and} \quad \frac{\partial}{\partial y}z(b) = -\frac{b_y}{b_z}. \tag{A2}$$

When (A2) is substituted in (A1), the result is

$$ub_x + vb_y + wb_z = w^*b_z.$$

Comparing this with the buoyancy equation in (2), we arrive at the expression for the cross-isopycnal flux:

$$w^* = \frac{D + B}{b_z}. \tag{A3}$$

The eddy-driven component thus readily isolated as

$$w^*_{\text{eddies}} = \frac{D}{b_z}, \tag{A4}$$

and (A4) is extensively used in diagnostics of our numerical experiments. The relative importance of eddies and small-scale mixing is measured by the ratio of the diapycnal fluxes in (A3) and (A4):

$$\alpha = \frac{\iint w^*_{\text{eddies}}\, dx\, dy}{\iint w^*\, dx\, dy}.$$

Its relatively large values ($\alpha \to 1$), realized in our direct numerical simulations, are indicative of the dominance of eddies in the integral buoyancy budget.

As we now show, $\alpha \to 1$ can only be achieved by *diabatic* eddies. Suppose for a moment that the eddies are adiabatic and $\overline{\mathbf{v}'b'} \cdot \nabla b = 0$. The integral of the time-mean buoyancy equation over a control volume V_T bounded by the base of the Ekman layer ($z = -h_{\text{Ek}}$) on top and by a time-mean isopycnal $b = b_0$ from below (see the discussion in section 2) is

$$\begin{aligned}\int \mathbf{v} \cdot \nabla b\, dV &= \int [-\nabla \cdot (\overline{\mathbf{v}'b'}) + B]\, dV \\ &= -\int_{b=b_0} \overline{\mathbf{v}'b'} \cdot \mathbf{n}\, dS - \int_{z=-h_{\text{Ek}}} \overline{w'b'}\, dx\, dy \\ &\quad + \int B\, dV. \end{aligned} \tag{A5}$$

Of the three terms in the rhs of (A5), the first is zero if the eddies are adiabatic, and the second is negligible since the vertical component of the eddy flux is suppressed by the proximity of the ocean surface. The third term, which may be written using (A3) (and noting that $b_z dz = db$) as $\int B\, dV = \int [(1 - \alpha) \int w^*\, dx\, dy]\, db$, is also asymptotically small for $\alpha \to 1$. Thus, for adiabatic eddies (A5) reduces to

$$\int \mathbf{v} \cdot \nabla b\, dV = \int w_{\text{Ek}}(b_S - b_0)\, dx\, dy = 0, \tag{A6}$$

where b_S is the surface buoyancy. Equation (A6) is impossible to satisfy for the control volume located in the subtropical gyre since $w_{\text{Ek}} < 0$ and $b_S > b_0$. This proves that eddies have to have a significant diabatic component in order to achieve large values of α, as is observed in our numerical simulations.

b. Potential vorticity

The large-scale potential vorticity defined in terms of the time-mean velocities $\mathbf{v}$, and time-mean buoyancy b, can be written, for a shallow-water fluid, thus:

$$\begin{aligned} Q &= (\nabla \times \mathbf{v} + f\mathbf{k}) \cdot \nabla b \\ &= \left(f + \frac{\partial v}{\partial x} - \frac{\partial u}{\partial y}\right)\frac{\partial b}{\partial z} - \frac{\partial v}{\partial z}\frac{\partial b}{\partial x} + \frac{\partial u}{\partial z}\frac{\partial b}{\partial y}, \end{aligned} \tag{A7}$$

where $\mathbf{k}$ is a unit vector in the vertical direction; Q should not be confused with the time mean of the potential vorticity based on the instantaneous velocity and buoyancy fields, which may differ because of the nonlinearity in (A7). Significance of the potential vorticity for the oceanic circulation is due to its quasi-conservative character and due to its invertibility that, under certain nonrestrictive assumptions, makes it possible to determine a unique distribution of velocity and density from the known PV field (Hoskins et al. 1985). Thus, knowledge of the factors that affect the PV dynamics may be crucial for understanding the time-mean ocean circulation.

A straightforward modification of the PV conservation theorem for the ideal flows (e.g., Pedlosky 1987) expresses the advective PV variation in terms of the diabatic terms:

$$\frac{D}{Dt}Q = \mathbf{v} \cdot \nabla Q = M_p + D_p + B_p, \tag{A8}$$

where

$$\begin{aligned} M_p &= (\nabla \times \mathbf{M}) \cdot \nabla b, \\ D_p &= (\nabla \times \mathbf{v} + f\mathbf{k}) \cdot \nabla D, \quad \text{and} \\ B_p &= (\nabla \times \mathbf{v} + f\mathbf{k}) \cdot \nabla B. \end{aligned} \tag{A9}$$

For the ideal flows [$M_u = M_v = D = B = 0$ in (2)] all terms on the right-hand side of (A8) vanish, and Q is conserved at any point advected by the mean velocity field:

$$\frac{D}{Dt}Q = 0.$$

Thus, the eddy terms M_u, M_v, and D, as well as the small-scale mixing B can be thought of as the internal sources and sinks of the mean field PV. The first component (M_p) is due to the Reynolds stress that generally tends to decelerate the relative rotation of the fluid (for a predominantly anticyclonic motion that would lead to increase in PV). The other mechanism, completely ab-

sent in homogeneous models, is due to eddy buoyancy transfer (D_p) acting to reduce the density gradients and thereby decrease PV. In this paper we quantify the relative contributions of each of these processes by diagnosing M_p and D_p from numerical simulations of the stratified eddying ocean flows.

First we rewrite the advective derivative D/Dt in a flux form:

$$\nabla \cdot (\mathbf{v}Q) = M_p + D_p + B_p. \tag{A10}$$

Equation (A10) is then integrated over a finite control volume V bounded by the closed surface S, and the left-hand side is reduced, using the Gauss theorem, to a surface integral over S:

$$\iint \mathbf{v}Q \cdot \mathbf{n}\, dS = \iiint M_p\, dV + \iiint D_p\, dV + \text{other terms}. \tag{A11}$$

Since B_p includes effects of both explicit and implicit numerical diffusion and the latter is rather difficult to accurately estimate, we make no attempt to diagnose B_p directly. The combined effect of all processes other than eddies [these are denoted in (A11) as the ''other terms''] will be computed as a difference between the surface flux of PV on the left-hand side of (A11) and the eddy terms on the right-hand side.

The eddy terms in (A10) can also be rewritten in a flux form using a generalized potential vorticity flux formulation, the so-called **J** vectors (Haynes and McIntyre 1987; Marshall and Nurser 1992), which is based on the following equivalent form of (A9):

$$M_p = \nabla \cdot (\mathbf{M} \times \nabla b) \quad \text{and}$$

$$D_p = \nabla \cdot [(\nabla \times \mathbf{v} + f\mathbf{k}) \cdot D].$$

Using the above, we replace the volume integrals in (A11) by fluxes through the bounding surface S:

$$\iint \mathbf{v}Q \cdot \mathbf{n}\, dS = \iint \mathbf{M} \times \nabla b \cdot \mathbf{n}\, dS \quad \text{and} + \iint (\nabla \times \mathbf{v} + f\mathbf{k}) D \cdot \mathbf{n}\, dS + \text{other terms}. \tag{A12}$$

An advantage of using (A12) to compute the global vorticity balances is its reduced order of derivatives, which renders the numerical diagnostic more robust. The form (A11), on the other hand, brings more insight into the life cycle of PV, directly indicating the spatial distribution of the large-scale PV modification due to eddies. Of course, these two forms are equivalent and the PV ''source'' terms in (A8) are equal to the divergence of the nonadvective component of **J** vectors in (A12). We make use of both forms, and the numerical results for the PV budgets agree within 1%.

The schematic in Fig. A1 defines the control volume over which we diagnose PV budget for the single-gyre

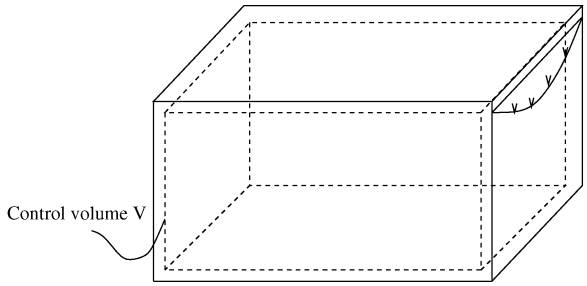

FIG. A1. Schematic of a control volume used in the diagnostics of potential vorticity. The volume is separated from the thin sublayers near the boundaries of the basin that are controlled by explicit diffusivity and viscosity.

model (section 3). This control volume is slightly separated from the rigid boundaries and surface. It is chosen to be outside the thin lateral sublayers controlled by explicit viscosity and diffusivity and the top and bottom Ekman layers (in our numerical simulations these sublayers are typically resolved by three grid points).

Since the stratification near the surface is much stronger than near the solid boundaries (see Fig. 1c), the PV flux on the left-hand side of (A11) is dominated by the contribution from the upper surface of the control volume. On the basis of this observation we rewrite (A11) as

$$\iint Q w_{\text{Ek}}\, dx\, dy = \iint dx\, dy \int M_p\, dz + \iint dx\, dy \int D_p\, dz + \text{other terms}, \tag{A13}$$

where the other terms now also include the PV fluxes through the lateral and bottom boundaries of the control volume. In order to estimate the partitioning of the PV budget, the Reynolds stress (M_u, M_v) and buoyancy transfer (D) terms are directly diagnosed from the numerical experiments and the integrals of M_p and D_p are then computed using both the flux formulation of (A12) and by direct integration of (A13).

Connection between the diapycnal buoyancy fluxes (w^*) and the PV dynamics appears when the equations of motion are written using buoyancy (rather than z) as a vertical coordinate. The PV equation in the isopycnal model [e.g., Pedlosky 1996, his Eq. (4.2.17)] is

$$\left.\frac{Dq}{Dt}\right|_b = q\frac{\partial w^*}{\partial z} + (\nabla \times \Im)\frac{\partial b}{\partial z},$$

where $q = (f + \zeta)/(\partial z/\partial b)$, $\zeta = \mathbf{k} \cdot \nabla \times \mathbf{v}$, and ($\Im_x$, $\Im_y$) are the isopycnal momentum dissipation terms. Thus PV variations due to the eddy buoyancy transfer can be thought of as a result of squeezing (stretching) of Taylor columns in each density layer layer by the diapycnal component of the vertical velocity ($\partial w^*/\partial z$).

REFERENCES

Bryan, K., 1996: The role of mesoscale eddies in the poleward transport of heat by the oceans: A review. *Physica D,* **98,** 249–257.

Chen, L. G., and W. K. Dewar, 1993: Intergyre communication in a three-layer model. *J. Phys. Oceanogr.,* **23,** 855–878.

Drijfhout, S. S., and W. Hazeleger, 2001: Eddy mixing of potential vorticity versus thickness in an isopycnic ocean model. *J. Phys. Oceanogr.,* **31,** 481–505.

Gent, P. R., and J. C. McWilliams, 1990: Isopycnal mixing in ocean circulation models. *J. Phys. Oceanogr.,* **20,** 150–155.

Haynes, P. H., and M. E. McIntyre, 1987: On the evolution of vorticity in the presence of diabatic heating and frictional or other forces. *J. Atmos. Sci.,* **44,** 828–841.

Hoskins, B. J., M. E. McIntyre, and A. W. Robertson, 1985: On the use and significance of isentropic potential vorticity maps. *Quart. J. Roy. Meteor. Soc.,* **111,** 877–946.

Hughes, C. W., 2002: An extra dimension to mixing. *Nature,* **416,** 136–139.

Karsten, R., H. Jones, and J. Marshall, 2002: The role of eddy transfer in setting the stratification and transport of a circumpolar current. *J. Phys. Oceanogr.,* **32,** 39–54.

Ledwell, J., A. Watson, and C. Law, 1993: Evidence for slow mixing across the pycnocline from an open-ocean tracer-release experiment. *Nature,* **367,** 701–703.

Marshall, J. C., 1984: Eddy mean flow interaction in a barotropic ocean model. *Quart. J. Roy. Meteor. Soc.,* **110,** 573–590.

——, and A. J. G. Nurser, 1992: Fluid dynamics of oceanic thermocline ventilation. *J. Phys. Oceanogr.,* **22,** 583–595.

——, ——, and R. G. Williams, 1993: Inferring the subduction rate and period over the North Atlantic. *J. Phys. Oceanogr.,* **23,** 1315–1329.

——, A. Adcroft, C. Hill, L. Perelman, and C. Heisey, 1997a: A finite-volume, incompressible Navier Stokes model for studies of the ocean on parallel computers. *J. Geophys. Res.,* **102** (C3), 5753–5766.

——, C. Hill, L. Perelman, and A. Adcroft, 1997b: Hydrostatic, quasi-hydrostatic, and nonhydrostatic ocean modeling. *J. Geophys. Res.,* **97,** 201–222.

——, H. Jones, R. Karsten, and R. Wardle, 2002: Can eddies set ocean stratification? *J. Phys. Oceanogr.,* **32,** 26–38.

McWilliams, J. C., G. Danabasoglu, and P. R. Gent, 1996: Tracer budgets in the warm water sphere. *Tellus,* **48,** 179–192.

Parsons, A. T., 1969: A two-layer model of Gulf Stream separation. *J. Fluid Mech.,* **39,** 511–528.

Pedlosky, J., 1987: *Geophysical Fluid Dynamics.* 2d ed. Springer-Verlag, 710 pp.

——, 1996: *Ocean Circulation Theory.* Springer-Verlag, 453 pp.

Radko, T., and J. Marshall, 2003: Equilibration of a warm pumped lens on a β plane. *J. Phys. Oceanogr.,* **33,** 885–899.

Rhines, P., 1993: Oceanic general circulation: Wave and advection dynamics. *Modelling Oceanic Climate Interactions,* J. Willebrand and D. L. T. Anderson, Eds., Springer-Verlag, 67–149.

Rintoul, S. R., C. W. Hughes, and D. Olbers, 2001: The Antarctic Circumpolar Current system. *Ocean Circulation and Climate,* G. Siedler, J. Church, and J. Gould, Eds., International Geophysical Series, Vol. 77, Academic Press, 271–302.